SIAM J. SCI. COMPUT.
Vol. 37, No. 4, pp. B591–B612

A DISCONTINUOUS GALERKIN FINITE ELEMENT METHOD FOR MULTIPHASE VISCOUS FLOW[*]

J. P. WHITELEY[†]

Abstract. Multiphase viscous flow is usually modeled by a coupled system of differential equations comprising hyperbolic partial differential equations describing the evolution of the volume fraction of each phase and elliptic partial differential equations describing quasi-static force balances. A discontinuous Galerkin finite element method is derived for this system of equations by appealing to conservation of flux and stress of each phase across element boundaries. One- and two-dimensional examples are used to demonstrate (i) the long-time stability of this method for problems where sharp gradients in solution variables develop as time evolves and (ii) the superiority of this technique over the continuous Galerkin finite element method for these exemplar problems.

Key words. multiphase flow, discontinuous Galerkin finite element, Stokes flow, hyperbolic PDEs

AMS subject classifications. 65N12, 65N30, 76T30

DOI. 10.1137/14098497X

1. Introduction.

Multiphase mixture theory has been used as a mathematical model for many applications, including paper manufacture [1], mushy layers [2], the manufacture of composite materials [3], tissue engineering [4], avascular tumour growth [5], vascular tumour growth [6], cell motility [7], and tissue development [8]. These models all assume that, at a given point in space, the mixture comprises two or more phases, with the overall composition of the mixture at a point in space determined by the local fractional contribution from each phase. For example, the vascular tumour model described by Breward, Byrne, and Lewis [6] includes three phases: tumour cells, extracellular material, and blood vessels. These local fractional contributions, commonly termed volume fractions, satisfy differential equations that are derived by appealing to conservation of mass. Each phase requires a constitutive relationship to specify a stress tensor, with common choices being the standard relationships for elastic solids, inviscid fluids, viscous fluids, and viscoelastic bodies. Conservation of momentum is then invoked to derive differential equations that relate the velocity or displacement of each phase to the forces acting on that phase.

Many applications have been underpinned by a multiphase mixture comprising two or more phases that are modeled as viscous fluids. Progress in understanding the model has usually been made by reducing the problem to one spatial dimension, allowing a numerical solution of the governing equations to be computed without requiring sophisticated numerical technqiues. This, however, prevents the investigation of two- and three-dimensional phenomena of interest such as, for example, shear stress dependent cell proliferation [9, 10, 11].

We shall see later that one feature of multiphase viscous flow models is that the volume fractions may exhibit very sharp gradients as time evolves. For sufficiently large time, these sharp gradients are effectively discontinuities when computed on a

---

[*] Submitted to the journal's Computational Methods in Science and Engineering section September 2, 2014; accepted for publication (in revised form) May 6, 2015; published electronically August 4, 2015.

http://www.siam.org/journals/sisc/37-4/98497.html

[†] Department of Computer Science, University of Oxford, Wolfson Building, Parks Road, Oxford OX1 3QD, UK (jonathan.whiteley@cs.ox.ac.uk).

finite element mesh with fixed element volume. It therefore seems appropriate to use a discontinuous Galerkin finite element method to calculate the numerical solution of the governing equations in these cases. Discontinuous Galerkin finite element methods have been shown to have many advantageous features, for example, (i) the stabilization of convection dominated problems [12, 13, 14], (ii) the availability of flexible *hp*-refinement strategies [15, 16, 14, 17, 13, 18, 19, 20, 21], (iii) the accuracy of the solution not being degraded by the use of highly anisotropic meshes [15, 16, 22], and (iv) the absence of locking for computing incompressible fluid flow [23, 24] and elastic deformations [25, 26, 20, 27, 22]. Using this approach, we do not assume that the solution is continuous across element boundaries. Instead, we assume the continuity of physical quantities such as the flux and stress of each phase. Furthermore, the volume fraction of each phase satisfies a first order hyperbolic partial differential equation. The discontinuous Galerkin finite element method therefore has the further advantage that this method readily permits stabilization of these hyperbolic equations.

In this study, we develop a discontinuous Galerkin finite element technique for multiphase viscous flow, which we demonstrate effectively handles the sharp interfaces in volume fractions that may develop as time evolves. We begin by writing down the governing equations for multiphase mixture theory in section 2 before deriving the finite element scheme in section 3. The use of this scheme is demonstrated in section 4, before concluding remarks are given in section 5.

2. The governing equations.

In this section, we write down the governing equations for the multiphase flow model that are used in subsequent sections of this study. For more details on these equations, see Lemon et al. [28].

2.1. The partial differential equations.

Suppose that a bounded domain Ω contains a mixture comprising N distinct phases. We assume that phase k, $k = 1, \dots, N$, occupies a fraction $0 \le \theta_k(\mathbf{x}, t) \le 1$ at every point $\mathbf{x} \in \Omega$ at time t, where $0 < t < T$ for some constant T. Assuming no voids in the mixture yields

$$\sum_{k=1}^{N} \theta_k = 1. \tag{2.1}$$

Denoting the velocity of phase k, $k = 1, 2, \dots, N$, by $\mathbf{u}_k$, and the density (assumed to be constant) by ρ_k, the volume fraction θ_k evolves according to, for $\mathbf{x} \in \Omega, 0 < t < T$:

$$\frac{\partial \theta_k}{\partial t} + \nabla \cdot (\theta_k \mathbf{u}_k) = \frac{1}{\rho_k} S_k(\theta_1, \dots, \theta_N), \qquad k = 1, 2, \dots, N, \tag{2.2}$$

where S_k is the net source term for phase k. Neglecting inertial terms, the conservation of momentum of phase k implies, for $\mathbf{x} \in \Omega, 0 < t < T$:

$$\nabla \cdot (\theta_k \boldsymbol{\sigma}_k) + \sum_{m \neq k} \mathbf{f}_{km} = \mathbf{0}, \qquad k = 1, 2, \dots, N, \tag{2.3}$$

where $\boldsymbol{\sigma}_k$ is the stress tensor for phase k, and $\mathbf{f}_{km}, m \neq k$ is the force exerted on phase k by phase m. Both $\boldsymbol{\sigma}_k$ and $\mathbf{f}_{km}, m \neq k$ are specified by constitutive relations which will be discussed in section 2.2. In (2.3), the first term requires a definition of the divergence of a tensor $\boldsymbol{\sigma}$: this is defined to be a vector, where entry i of this vector is given by

$$(\nabla \cdot \boldsymbol{\sigma})_i = \sum_j \frac{\partial \sigma_{ij}}{\partial x_j}.$$

2.2. Constitutive relationships. We now write down a general set of constitutive relationships for the multiphase mixture model. The interphase pressure between phases k and m, p_{km}, is given by

$$p_{km} = p + \psi_{km}\left(\theta_1, \theta_2, \ldots, \theta_N\right), \qquad k, m = 1, 2, \ldots, N, \qquad m \neq k,$$

where ψ_{km} is the interphase traction between phases k and m and satisfies

$$\psi_{km} = \psi_{mk}, \tag{2.4}$$

and p is the mixture pressure. The force exerted on phase k by phase m is then given by

$$\mathbf{f}_{km} = p_{km}\theta_m \nabla\theta_k - p_{mk}\theta_k \nabla\theta_m + \beta_{km}\theta_k\theta_m\left(\mathbf{u}_m - \mathbf{u}_k\right), \qquad m \neq k, \tag{2.5}$$

where the constants $\beta_{km} = \beta_{mk} > 0$ represent the viscous drag between phase k and phase m. The summation in (2.3) becomes, on using (2.1) and (2.4),

$$\sum_{m\neq k} \mathbf{f}_{km} = p\nabla\theta_k + \sum_{m\neq k} \psi_{km}\left(\theta_m\nabla\theta_k - \theta_k\nabla\theta_m\right) + \sum_{m\neq k} \beta_{km}\theta_k\theta_m\left(\mathbf{u}_m - \mathbf{u}_k\right). \tag{2.6}$$

Finally, the stress tensor for each phase is determined by specifying the class of fluid or solid the phase belongs to. In this study, we consider phases that may be modeled as viscous fluids, and so the stress tensor of phase k may be written

$$\boldsymbol{\sigma}_k = -p_k\mathcal{I} + \mathcal{D}_k, \tag{2.7}$$

where $\mathcal{I}$ is the identity tensor, the pressure of phase k, p_k, is given by

$$p_k = p + \Sigma_k\left(\theta_1, \theta_2, \ldots, \theta_N\right) + \sum_{m\neq k} \theta_m\psi_{km}\left(\theta_1, \theta_2, \ldots, \theta_N\right)$$

for a specified function Σ_k and $\mathcal{D}_k$, is the deviatoric component of the stress tensor. For a viscous fluid, $\mathcal{D}_k$ is given by

$$\mathcal{D}_k = \mu_k\left(\nabla\mathbf{u}_k + \left(\nabla\mathbf{u}_k\right)^\top\right) + \lambda_k\left(\nabla\cdot\mathbf{u}_k\right)\mathcal{I},$$

where μ_k is the shear viscosity of phase k, $\lambda_k = -2\mu_k/3$ is the bulk viscosity of phase k, and the gradient of a vector $\mathbf{u}$ is defined to be the tensor with entries given by

$$\left(\nabla\mathbf{u}\right)_{ij} = \frac{\partial u_i}{\partial x_j}.$$

2.3. Initial conditions. Initial conditions are required for the volume fraction of each phase:

$$\theta_k(\mathbf{x}, 0) = \theta_k^{(0)}(\mathbf{x}), \qquad k = 1, 2, \ldots, N, \qquad \mathbf{x} \in \Omega, \tag{2.8}$$

where $\theta_k^{(0)}(\mathbf{x}), k = 1, 2, \ldots, N$, are specified functions that satisfy the no voids condition, (2.1), i.e.,

$$\sum_{k=1}^{N} \theta_k^{(0)}(\mathbf{x}) = 1, \qquad \mathbf{x} \in \Omega. \tag{2.9}$$

2.4. Boundary conditions. At each point on the boundary $\partial\Omega$, we must specify either the velocity (a Dirichlet boundary condition) or the traction (a Neumann boundary condition) in all coordinate directions for each phase. For phase k, a Dirichlet boundary condition is given by

$$\mathbf{u}_k(\mathbf{x},t) = \mathbf{v}_k(\mathbf{x},t), \qquad \mathbf{x} \in \partial\Omega_{D,k}, \qquad 0 < t < T, \tag{2.10}$$

and a Neumann boundary condition is given by

$$\theta_k \boldsymbol{\sigma}_k \mathbf{n} = \mathbf{s}_k(\mathbf{x},t), \qquad \mathbf{x} \in \partial\Omega_{N,k}, \qquad 0 < t < T, \tag{2.11}$$

where $\mathbf{n}$ is the outward pointing unit normal to Ω, the sets $\partial\Omega_{D,k}$, $\partial\Omega_{N,k}$ are the subsets of the boundaries where Dirichlet and Neumann boundary conditions are applied for phase k, and $\mathbf{v}_k$ and $\mathbf{s}_k$ are specified functions.

At a point $\mathbf{x}$ on the boundary $\partial\Omega$, the boundary is an inflow boundary for phase k if $\mathbf{u}_k \cdot \mathbf{n} < 0$. We denote the inflow boundary for phase k by $\partial\Omega_k^-$. The volume fraction for phase k must be specified on $\partial\Omega_k^-$, i.e.,

$$\theta_k(\mathbf{x},t) = \theta_k^-(\mathbf{x},t), \qquad \mathbf{x} \in \partial\Omega_k^-, \qquad 0 < t < T, \tag{2.12}$$

where θ_k^- is a specified function.

2.5. Manipulation of the governing equations. We may manipulate (2.1) and (2.2) to allow us to rewrite these equations in a form that allows easier application of the finite element method. Summing (2.2) over all phases, we obtain

$$\frac{\partial}{\partial t}\left(\sum_{k=1}^{N} \theta_k\right) + \nabla \cdot \left(\sum_{k=1}^{N} \theta_k \mathbf{u}_k\right) = \sum_{k=1}^{N} \frac{S_k}{\rho_k}. \tag{2.13}$$

Provided the initial no-voids condition, (2.9), is satisfied, we see from (2.13) that the no-voids condition, (2.1), is satisfied for all time provided the velocities of the phases satisfy

$$\nabla \cdot \left(\sum_{k=1}^{N} \theta_k \mathbf{u}_k\right) = \sum_{k=1}^{N} \frac{S_k}{\rho_k}. \tag{2.14}$$

We can think of the pressure p as being a Lagrange multiplier that enforces the constraint given by (2.14) in the same way that the pressure calculated from the Navier–Stokes equations enforces the incompressibility constraint for a homogeneous (single phase) fluid. For the remainder of this paper, we shall work with this system of equations given by (2.2), (2.3), (2.14) subject to the initial conditions given by (2.8), the boundary conditions given by (2.10), (2.11), and (2.12), and the constitutive relations given in section 2.2.

3. Derivation of the discontinuous Galerkin finite element method.

We now develop the discontinuous Galerkin finite element method for solving (2.2), (2.3), (2.14), the equations governing multiphase viscous flow. We define the mathematical machinery required in section 3.1 and justify the physical quantities that we conserve across element boundaries in section 3.2. We then derive a weak formulation of (2.3) and (2.14) in section 3.3. In section 3.4, the weak solution of (2.3) and (2.14) is used to write down a discontinuous Galerkin finite element method for these equations. This is combined with the discontinuous Galerkin finite element method for hyperbolic conservation laws derived by Hartmann and Houston [14] for solving (2.2), allowing us to write down the finite element scheme for the coupled system of equations given by (2.2), (2.3), (2.14). We then describe how this finite element scheme may be uncoupled in section 3.5.

3.1. Mathematical preliminaries. The space of square integrable functions on the spatial domain Ω, $L_2(\Omega)$, and the Sobolev space of order 1, $H^1(\Omega)$, are defined by

$$L^2(\Omega) = \left\{ v : \int_\Omega v^2 \ \mathrm{d}V < \infty \right\},$$
$$H^1(\Omega) = \left\{ v \in L^2(\Omega) : \frac{\partial v}{\partial x_i} \in L^2(\Omega), i = 1, \dots, d \right\},$$

where d is the number of spatial dimensions. Let $\mathcal{T}_h = \{e\}$ be a mesh that partitions Ω into quadrilateral elements (in two dimensions) or hexahedral elements (in three dimensions) denoted by e. The broken Sobolev space of order 1, $H^1(\Omega, \mathcal{T}_h)$, is defined by

$$H^1(\Omega, \mathcal{T}_h) = \{u \in L_2(\Omega) : u \mid_\alpha \in H^1(\alpha) \ \forall \alpha \in \mathcal{T}_h\}.$$

We define $Q^k(\Omega)$ to be set of functions that are tensor product polynomials of degree k when restricted to a given element. Function spaces for vector valued functions are specified by, for example, $[L_2(\Omega)]^2 = L_2(\Omega) \times L_2(\Omega)$.

The boundary of any $e \in \mathcal{T}_h$ is denoted by ∂e. On ∂e, we define v_e^+, the interior trace of any $v \in H^1(e)$, to be the trace taken from within e. If $\partial e - \partial\Omega$ is not empty, then for any $\mathbf{x} \in \partial e - \partial\Omega$ there exists a unique element $e' \neq e$ such that $\mathbf{x} \in e'$. We define v_e^-, the exterior trace of $v \in H^1(e)$ relative to e, by the trace taken from within e'. If $\partial e \cap \partial\Omega_D$ is not empty, then for $\mathbf{x} \in \partial e \cap \partial\Omega_D$ the exterior trace v_e^- is defined by Dirichlet boundary conditions on v if this boundary condition is specified. For any $v \in H^1(e)$, if v_e^- exists at $\mathbf{x} \in \partial e$, the jump, $[v]_e$, across ∂e relative to e, and the mean value $\langle v \rangle_e$ are defined by

$$[v]_e = v_e^+ - v_e^-,$$
$$\langle v \rangle_e = \frac{1}{2}\left(v_e^+ + v_e^-\right).$$

The outward pointing unit normal to the element e is denoted by $\mathbf{n}_e$.

3.2. Continuity across element boundaries. For phase k, $k = 1, 2, \dots, N$, continuity of flux of phase k across and along both interior element boundaries (i.e., element boundaries shared by two elements) and the intersection between element boundaries and Dirichlet boundaries for phase k, $\partial\Omega_{D,k}$ yields

$$[\theta_k \mathbf{u_k}] = \mathbf{0}, \qquad k = 1, 2, \dots, N, \qquad \mathbf{x} \in \partial e - \partial\Omega_{N,k}, \tag{3.1}$$

and continuity of the stress of phase k across the same element boundaries yields

$$[\theta_k \boldsymbol{\sigma_k}]\mathbf{n}_e = \mathbf{0}, \qquad k = 1, 2, \dots, N, \qquad \mathbf{x} \in \partial e - \partial\Omega_{N,k}. \tag{3.2}$$

In section 3.3, we shall impose (3.1) and (3.2) weakly when deriving the weak solution of (2.3) and (2.14).

3.3. The weak solution of (2.3) and (2.14). Suppose we have a vector valued function $\boldsymbol{\phi_k} \in [H^1(\Omega, \mathcal{T}_h)]^d$, where d is the number of spatial dimensions. Taking the scalar product of (2.3) with $\boldsymbol{\phi_k}$, integrating over Ω, applying the divergence theorem, and using the constitutive relations given by (2.5), (2.6), (2.7) yields

$$\begin{aligned}\sum_e \int_e \theta_k \mathbf{D_k} : \nabla \boldsymbol{\phi_k} + \sum_{m \neq k} \beta_{km} \theta_k \theta_m \left(\mathbf{u_k} - \mathbf{u_m}\right) \cdot \boldsymbol{\phi_k} - p \nabla \cdot (\theta_k \boldsymbol{\phi_k}) \\ - g_{1,k} \nabla \cdot \boldsymbol{\phi_k} + \mathbf{g_{2,k}} \cdot \boldsymbol{\phi_k} \ \mathrm{d}V - \sum_e \int_{\partial e} \boldsymbol{\phi_k} \cdot \left(\theta_k \boldsymbol{\sigma_k} \mathbf{n}_e\right) \ \mathrm{d}S = 0,\end{aligned} \tag{3.3}$$

where $\mathbf{S} : \mathbf{T} = \sum_{i,j} S_{ij} T_{ij}$, and

$$\begin{aligned} g_{1,k}(\theta_1, \ldots, \theta_N) &= \theta_k \Sigma_k + \sum_{m \neq k} \theta_k \theta_m \psi_{km}, \\ \mathbf{g_{2,k}}(\theta_1, \ldots, \theta_N) &= \sum_{m \neq k} \psi_{km} \left(\theta_k \nabla \theta_m - \theta_m \nabla \theta_k\right). \end{aligned}$$

We now use the continuity conditions for phase k, given by (3.1) and (3.2), and the Neumann boundary conditions, (2.11), to rewrite the surface integral in (3.3):

$$\begin{aligned} \int_{\partial e} \boldsymbol{\phi_k} \cdot \left(\theta_k \boldsymbol{\sigma_k} \mathbf{n}_e\right) \ \mathrm{d}S &= \int_{\partial e - \partial \Omega_N} \boldsymbol{\phi_k} \cdot \left(\theta_k \boldsymbol{\sigma_k} \mathbf{n}_e\right) \ \mathrm{d}S \\ &\quad + \int_{\partial e \cap \Omega_N} \boldsymbol{\phi_k} \cdot \left(\theta_k \boldsymbol{\sigma_k} \mathbf{n}_e\right) \ \mathrm{d}S \\ &= \int_{\partial e - \partial \Omega_N} \boldsymbol{\phi_k} \cdot \left(\langle \theta_k \boldsymbol{\sigma_k} \rangle \mathbf{n}_e\right) \ \mathrm{d}S + \int_{\partial e \cap \Omega_N} \boldsymbol{\phi_k} \cdot \mathbf{s}_k \ \mathrm{d}S \\ &= \int_{\partial e - \partial \Omega_N} \boldsymbol{\phi_k} \cdot \left(\langle \theta_k \boldsymbol{\sigma_k} \rangle \mathbf{n}_e\right) - \frac{C_u}{h_{\partial e}} [\theta_k \mathbf{u_k}] \cdot \boldsymbol{\phi_k} \ \mathrm{d}S \\ &\quad + \int_{\partial e \cap \Omega_N} \boldsymbol{\phi_k} \cdot \mathbf{s}_k \ \mathrm{d}S \\ &= \int_{\partial e - \partial \Omega_N} \boldsymbol{\phi_k} \cdot \big(\langle \theta_k \mathbf{D_k} \rangle \mathbf{n}_e - \langle \theta_k p + g_{1,k} \rangle \mathbf{n}_e \\ &\qquad - \frac{C_u}{h_{\partial e}} [\theta_k \mathbf{u_k}] \big) \ \mathrm{d}S + \int_{\partial e \cap \Omega_N} \boldsymbol{\phi_k} \cdot \mathbf{s}_k \ \mathrm{d}S, \end{aligned} \tag{3.4}$$

where $C_u > 0$ is a sufficiently large constant, and $h_{\partial e}$ is the diameter of the edge of e. We may also write

$$\int_e p \nabla \cdot (\theta_k \boldsymbol{\phi_k}) \ \mathrm{d}V = \int_{\partial e} p \theta_k \boldsymbol{\phi_k} \cdot \mathbf{n}_e \ \mathrm{d}S - \int_e (\nabla p) \cdot (\theta_k \boldsymbol{\phi_k}) \ \mathrm{d}V. \tag{3.5}$$

Using (3.4) and (3.5), (3.3) becomes, for all $\boldsymbol{\phi_k} \in [H^1(\Omega, \mathcal{T}_h)]^d$,

$$A_k(\mathbf{u_1}, \ldots, \mathbf{u_N}, p, \theta_1, \ldots, \theta_N, \boldsymbol{\phi_k}) + E_k(\theta_1, \ldots, \theta_N, \boldsymbol{\phi_k}) + l_k(\boldsymbol{\phi_k}) = 0, \tag{3.6}$$

where

$$
\begin{aligned}
&A_k(\mathbf{u_1},\dots,\mathbf{u_N},p,\theta_1,\dots,\theta_N,\boldsymbol{\phi_k})\\
&\quad=\sum_e\int_e \theta_k\mathbf{D_k}:\nabla\boldsymbol{\phi_k}+\sum_{m\neq k}\beta_{km}\theta_k\theta_m\left(\mathbf{u_k}-\mathbf{u_m}\right)\cdot\boldsymbol{\phi_k}\ \mathrm{d}V\\
&\qquad+\sum_e\int_{\partial e-\partial\Omega_N}\boldsymbol{\phi_k}\cdot\left(\frac{C_u}{h_{\partial e}}[\theta_k\mathbf{u_k}]-\langle\theta_k\mathbf{D_k}\rangle\mathbf{n}_e\right)\ \mathrm{d}S\\
&\qquad+\sum_e\int_e(\nabla p)\cdot(\theta_k\boldsymbol{\phi_k})\ \mathrm{d}V\\
&\qquad+\sum_e\int_{\partial e-\partial\Omega_N}\langle\theta_k p\rangle\boldsymbol{\phi_k}\cdot\mathbf{n}_e\ \mathrm{d}S-\sum_e\int_{\partial e}p\theta_k\boldsymbol{\phi_k}\cdot\mathbf{n}_e\ \mathrm{d}S,
\end{aligned}
\tag{3.7}
$$

$$
\begin{aligned}
&E_k(\theta_1,\dots,\theta_N,\boldsymbol{\phi_k})\\
&\quad=\sum_e\int_e -g_{1,k}\nabla\cdot\boldsymbol{\phi_k}+\mathbf{g_{2,k}}\cdot\boldsymbol{\phi_k}\ \mathrm{d}V\\
&\qquad+\sum_e\int_{\partial e-\partial\Omega_N}\langle g_{1,k}\rangle\boldsymbol{\phi_k}\cdot\mathbf{n}_e\ \mathrm{d}S,
\end{aligned}
\tag{3.8}
$$

$$
l_k(\boldsymbol{\phi_k})=-\sum_e\int_{\partial e\cap\Omega_N}\boldsymbol{\phi_k}\cdot\mathbf{s}_k\ \mathrm{d}S.
\tag{3.9}
$$

We now turn our attention to the weak solution of (2.14). If $\psi\in H^1(\Omega,\mathcal{T}_h)$, then multiplying (2.14) by ψ, integrating over Ω, and applying the divergence theorem implies that

$$
\sum_e\left(-\int_e\left(\sum_{k=1}^N\theta_k\mathbf{u_k}\right)\cdot\nabla\psi+\psi\sum_{k=1}^N\frac{S_k}{\rho_k}\ \mathrm{d}V+\int_{\partial e}\psi\sum_{k=1}^N\theta_k\mathbf{u_k}\cdot\mathbf{n}_e\ \mathrm{d}S\right)=0.
\tag{3.10}
$$

Using the continuity of flux of each phase, (3.1), allows us to write (3.10) as

$$
B(\mathbf{u_1},\dots,\mathbf{u_N},\theta_1,\dots,\theta_N,\psi)=0,
\tag{3.11}
$$

where

$$
\begin{aligned}
&B(\mathbf{u_1},\dots,\mathbf{u_N},\theta_1,\dots,\theta_N,\psi)\\
&\quad=-\sum_e\int_e\left(\sum_{k=1}^N\theta_k\mathbf{u_k}\right)\cdot\nabla\psi+\psi\sum_{k=1}^N\frac{S_k}{\rho_k}\ \mathrm{d}V\\
&\qquad+\sum_{k=1}^N\left(\sum_e\int_{\partial e\cap\partial\Omega_{N,k}}\psi\theta_k\mathbf{u_k}\cdot\mathbf{n}_e\ \mathrm{d}S+\sum_e\int_{\partial e-\partial\Omega_{N,k}}\psi\langle\theta_k\mathbf{u_k}\rangle\cdot\mathbf{n}_e\ \mathrm{d}S\right).
\end{aligned}
\tag{3.12}
$$

If $\theta_1,\theta_2,\dots,\theta_N$ are known for some time t, the weak solution of (2.3) and (2.14) for $\mathbf{u_1},\mathbf{u_2},\dots,\mathbf{u_N},p$ at this time satisfies (3.6) for all $\boldsymbol{\phi_k}\in[H^1(\Omega,\mathcal{T}_h)]^d$, $k=1,2,\dots,N$, and (3.11) for all $\psi\in H^1(\Omega,\mathcal{T}_h)$.

3.4. The coupled discontinuous Galerkin finite element scheme.

We now write down a discontinuous Galerkin finite element method for the solution of (2.2), (2.3), and (2.14). The discretization of (2.2) is an adaptation of the method described by Hartmann and Houston [14], and the discretization of (2.3) and (2.14) is based on the weak solution derived in section 3.3.

We shall use the subscript "h" for all solution variables appearing in the finite element solution and compute the finite element solution for all solution variables at times t_n, $n = 0, 1, 2, \dots$, where $t_0 = 0$ and $t_{n+1} > t_n$ for $n = 0, 1, 2, \dots$. We use the superscript "(n)" to represent the solution at time t_n, so, for example,

$$\theta_{k,h}^{(n)}(x) = \theta_{k,h}(x, t_n), \qquad k = 1, 2, \dots, N, \qquad n = 0, 1, 2, \dots.$$

In common with other authors [10, 11], we shall seek a finite element solution with $\mathbf{u_{k,h}}^{(n)} \in \left[Q^2(\Omega)\right]^d$, $k = 1, \dots, N$, and $p_h^{(n)} \in Q^1(\Omega)$. We shall also seek a finite element solution $\theta_{k,h}^{(n)} \in Q^1(\Omega)$, $k = 1, \dots, N$.

We note that $\theta_k^{(0)}$, $k = 1, 2, \dots, N$, is given by the initial conditions, (2.8). We then discretize (2.2) in time implicitly to give

$$\nabla \cdot \left(\theta_k^{(n)} \mathbf{u_k}^{(n)}\right) + \frac{\theta_k^{(n)} - \theta_k^{(n-1)}}{t_n - t_{n-1}} - \frac{S_k(\theta_1^{(n)}, \dots, \theta_N^{(n)})}{\rho_k} = 0.$$

We now discretize the divergence operator in the same manner as Hartmann and Houston [14] to give the finite element solution of (2.2) as follows: find $\theta_{k,h} \in Q^1(\Omega)$, such that for all $\chi_k \in Q^1(\Omega)$, we have, for $k = 1, 2, \dots, N$ and $n = 1, 2, \dots$

$$C_k(\mathbf{u_{1,h}}^{(n)}, \dots, \mathbf{u_{N,h}}^{(n)}, \theta_{1,h}^{(n)}, \dots, \theta_{N,h}^{(n)}, \theta_{1,h}^{(n-1)}, \dots, \theta_{N,h}^{(n-1)}, \chi_k) = 0, \tag{3.13}$$

where

$$\begin{aligned} &C_k(\mathbf{u_{1,h}}^{(n)}, \dots, \mathbf{u_{N,h}}^{(n)}, \theta_{1,h}^{(n)}, \dots, \theta_{N,h}^{(n)}, \theta_{1,h}^{(n-1)}, \dots, \theta_{N,h}^{(n-1)}, \chi_k) \\ &\quad = \sum_e \Bigg(\int_e -\theta_{k,h}^{(n)} \mathbf{u_{k,h}}^{(n)} \cdot \nabla \chi_k + \delta_k \nabla \theta_{k,h}^{(n)} \cdot \nabla \chi_k \\ &\qquad\qquad + \left(\frac{\theta_{k,h}^{(n)} - \theta_{k,h}^{(n-1)}}{t_n - t_{n-1}} - \frac{S_k(\theta_{1,h}^{(n)}, \dots, \theta_{N,h}^{(n)})}{\rho_k} \right) \chi_k \ \mathrm{d}V \\ &\qquad\qquad + \int_{\partial e \cap \partial \Omega_{N,k}} \theta_{k,h}^{(n)} \mathbf{u_{k,h}}^{(n)} \cdot \mathbf{n}_e \chi_k^+ \ \mathrm{d}S \\ &\qquad\qquad + \int_{\partial e - \partial \Omega_{N,k}} \left(\langle \theta_{k,h}^{(n)} \mathbf{u_{k,h}}^{(n)} \rangle \cdot \mathbf{n}_e + \alpha_k [\theta_{k,h}^{(n)}] \right) \chi_k^+ \ \mathrm{d}S \Bigg), \end{aligned} \tag{3.14}$$

and

$$\delta_k = C_\delta h^{2-\beta} \left| \nabla \cdot \left(\theta_{k,h}^{(n)} \mathbf{u_{k,h}}^{(n)} \right) \right|$$

for constants $C_\delta > 0$ and $0 < \beta < 0.5$, and where h is a mesh function, in this case the diameter of the element. The parameters α_k, $k = 1, 2, \dots, N$ are positive constants that are defined by the analysis of Hartmann and Houston [14].

The coupled discontinuous Galerkin finite element scheme is then given by the following: for $n = 1, 2, 3, \dots$, find $\mathbf{u_{k,h}}^{(n)} \in [Q^2(\Omega)]^d$, $k = 1, 2, \dots, N$, $p_h^{(n)} \in Q^1(\Omega)$, $\theta_{k,h}^{(n)} \in Q^1(\Omega)$, $k = 1, 2, \dots, N$ such that, for all $\boldsymbol{\phi_k} \in [Q^2(\Omega)]^d$, $k = 1, 2, \dots, N$,

$\psi \in Q^1(\Omega)$, $\chi_k \in Q^1(\Omega)$, $k = 1, 2, \ldots, N$,

$$A_k(\mathbf{u_{1,h}}^{(n)}, \ldots, \mathbf{u_{N,h}}^{(n)}, p_h^{(n)}, \theta_{1,h}^{(n)}, \ldots, \theta_{N,h}^{(n)}, \boldsymbol{\phi_k}) \\ + E_k(\theta_{1,h}^{(n)}, \ldots, \theta_{N,h}^{(n)}, \boldsymbol{\phi_k}) + l_k(\boldsymbol{\phi_k}) = 0, \tag{3.15}$$

$$B(\mathbf{u_{1,h}}^{(n)}, \ldots, \mathbf{u_{N,h}}^{(n)}, \theta_{1,h}^{(n)}, \ldots, \theta_{N,h}^{(n)}, \psi) = 0, \tag{3.16}$$

$$C_k(\mathbf{u_{1,h}}^{(n)}, \ldots, \mathbf{u_{N,h}}^{(n)}, \theta_{1,h}^{(n)}, \ldots, \theta_{N,h}^{(n)}, \theta_{1,h}^{(n-1)}, \ldots, \theta_{N,h}^{(n-1)}, \chi_k) = 0, \tag{3.17}$$

where A_k, B, C_k, E_k, l_k are given by (3.7), (3.12), (3.14), (3.8), (3.9). We use the word "coupled" to describe this scheme as the volume fraction of all phases, the velocity of all phases, and the common pressure are all computed from a fully coupled system on each timestep.

3.5. The uncoupled discontinuous Galerkin finite element scheme.

In contrast to the coupled discontinuous Galerkin finite element scheme presented in section 3.4, other authors [10, 11] have computed a finite element solution where on each timestep the velocity of each phase and the pressure are updated first, based on the volume fractions at the previous timestep. The volume fraction of each phase is then updated based on these velocities and pressure. This may be achieved by uncoupling the calculation of the volume fraction of each phase from the coupled discontinuous Galerkin finite element scheme given by (3.15), (3.16), (3.17). The uncoupled discontinuous Galerkin finite element method is given by: for $n = 1, 2, 3, \ldots$, find $\mathbf{u_{k,h}}^{(n)} \in [Q^2(\Omega)]^d$, $k = 1, 2, \ldots, N$, $p_h^{(n)} \in Q^1(\Omega)$, $\theta_{k,h}^{(n)} \in Q^1(\Omega)$, $k = 1, 2, \ldots, N$ such that, for all $\boldsymbol{\phi_k} \in [Q^2(\Omega)]^d$, $k = 1, 2, \ldots, N$, $\psi \in Q^1(\Omega)$, $\chi_k \in Q^1(\Omega)$, $k = 1, 2, \ldots, N$,

$$A_k(\mathbf{u_{1,h}}^{(n)}, \ldots, \mathbf{u_{N,h}}^{(n)}, p_h^{(n)}, \theta_{1,h}^{(n-1)}, \ldots, \theta_{N,h}^{(n-1)}, \boldsymbol{\phi_k}) \\ + E_k(\theta_{1,h}^{(n-1)}, \ldots, \theta_{N,h}^{(n-1)}, \boldsymbol{\phi_k}) + l_k(\boldsymbol{\phi_k}) = 0, \tag{3.18}$$

$$B(\mathbf{u_{1,h}}^{(n)}, \ldots, \mathbf{u_{N,h}}^{(n)}, \theta_{1,h}^{(n-1)}, \ldots, \theta_{N,h}^{(n-1)}, \psi) = 0, \tag{3.19}$$

$$C_k(\mathbf{u_{1,h}}^{(n)}, \ldots, \mathbf{u_{N,h}}^{(n)}, \theta_{1,h}^{(n)}, \ldots, \theta_{N,h}^{(n)}, \theta_{1,h}^{(n-1)}, \ldots, \theta_{N,h}^{(n-1)}, \chi_k) = 0, \tag{3.20}$$

where A_k, B, C_k, E_k, l_k are given by (3.7), (3.12), (3.14), (3.8), (3.9). Using this approach we see that (3.18) and (3.19) are independent of $\theta_{1,h}^{(n)}, \theta_{2,h}^{(n)}, \ldots, \theta_{N,h}^{(n)}$, and so the velocity of each phase and pressure at time $t = t_n$ can be calculated independently of the volume fraction of each phase at time $t = t_n$.

4. Numerical simulations.

We now demonstrate the use of the discontinuous Galerkin finite element method presented in this study. Our first computations, in section 4.1, use examples with one spatial dimension to show that our method is appropriate for handling the sharp gradients in volume fractions, highlighted in section 1, that may emerge as time evolves. We then demonstrate in section 4.2 the limitations of using a continuous Galerkin finite element method for these simulations. Finally, in section 4.3, we present example two-dimensional computations that exhibit sharp gradients in volume fraction, and we verify that the discontinuous Galerkin finite element method derived earlier is also suitable for these problems.

4.1. One-dimensional computations using the discontinuous Galerkin finite element method.

We begin by using the discontinuous Galerkin finite element approximation derived earlier for one-dimensional, two-phase viscous flow. In order to demonstrate sharp gradients that may appear in the volume fractions of the phases, we use an example motivated by a mathematical model of biological cells. In this model, cells, which will be termed phase 1, are mixed with a second phase that models extracellular material; see, for example, [6, 9, 10, 28] for more details on modeling cells in this manner. Appropriate constitutive relations are given by

$$\begin{aligned} &\psi_{12} = 0, \\ &\Sigma_1 = \Gamma \frac{\theta_1 - \theta_1^*}{(1-\theta_1)^2} + \Lambda \left(\left(\frac{\epsilon}{x}\right)^n - \left(\frac{\epsilon}{x}\right)^m \right), \\ &\Sigma_2 = 0, \end{aligned} \tag{4.1}$$

where Γ, θ_1^*, Λ, ϵ, $n > m > 0$ are given constants. Unless otherwise stated, the parameters we use are given by $\rho_1 = \rho_2 = 1$, $S_1 = S_2 = 0$, $\beta_{12} = 1$, $\mu_1 = \mu_2 = 1$, $\Gamma = 1$, $\theta_1^* = 0.3$, $\Lambda = 10^5$, $\epsilon = 10^{-5}$, $n = 10$, $m = 2$. The domain Ω is defined by the interval $0 < x < 1$. Boundary conditions are given by $u_1 = u_2 = 0$ at $x = 0, 1$. Initial conditions at time $t = 0$ are given by, for $0 < x < 1$,

$$\begin{aligned} \theta_1(x, 0) &= 0.1 + 0.05 \sin \pi x, \\ \theta_2(x, 0) &= 1 - \theta_1(x, 0). \end{aligned}$$

The function Σ_1 that models the extra pressure in the cell phase, and has been defined by (4.1), deserves more explanation. The first term on the right-hand side of this equation models the tendency of cells to aggregate for low θ_1 (hence the low value of this expression as θ_1 approaches 0) and to repel other cells for high θ_1 (hence the high value as θ_1 approaches 1). The second term is, in effect, a penalty term to prevent θ_1 ever actually reaching the value of zero. The rationale for this can be seen from (2.3) and (2.5): should θ_1 take the value zero, then (2.3) would reduce to the singular system $\mathbf{0} = \mathbf{0}$, and we would be unable to determine the velocity $\mathbf{u}_1$ of this phase. This is consistent with the physical processes being modeled: if a volume fraction θ_k ever reaches zero at a point, then phase k does not exist at this point. The velocity $\mathbf{u}_k$ is then meaningless. This could, of course, be modeled as a moving boundary value problem where a phase only exists in the subset of Ω where it has a positive volume fraction. However, this would be very hard to implement in two or three dimensions. Instead, we introduce the second term in (4.1). This term has negligible effect for $\theta_1 > \epsilon$ but becomes large and positive as θ_1 approaches zero, thus generating a high pressure and ensuring that the solution for θ_1 never reaches zero. This penalty function approach has been used before for modeling an evaporating fluid [29]. We will investigate the effect of not including this function by setting $\Lambda = 0$ later in this section. Unless otherwise stated, all computations presented are generated using a timestep of 0.01.

4.1.1. The coupled discontinuous Galerkin finite element method. We begin by using the coupled discontinuous Galerkin finite element method given by (3.15), (3.16), and (3.17). Our first computation uses 1000 equally sized elements to calculate the coupled discontinuous Galerkin finite element approximation of the model problem described in section 4.1. The volume fraction of the cell phase, denoted by θ_1, is plotted in Figure 1(a) for times $t = 0, 5, 10, 15, 20, 25$, where we see that as time evolves the solution begins to develop sharp gradients that separate regions where θ_1 is very small from regions with a significant cell occupation. The solution is then plotted in Figure 1(b) for time $t = 30$, Figure 1(c) for time $t = 40$, and Figure 1(d) for

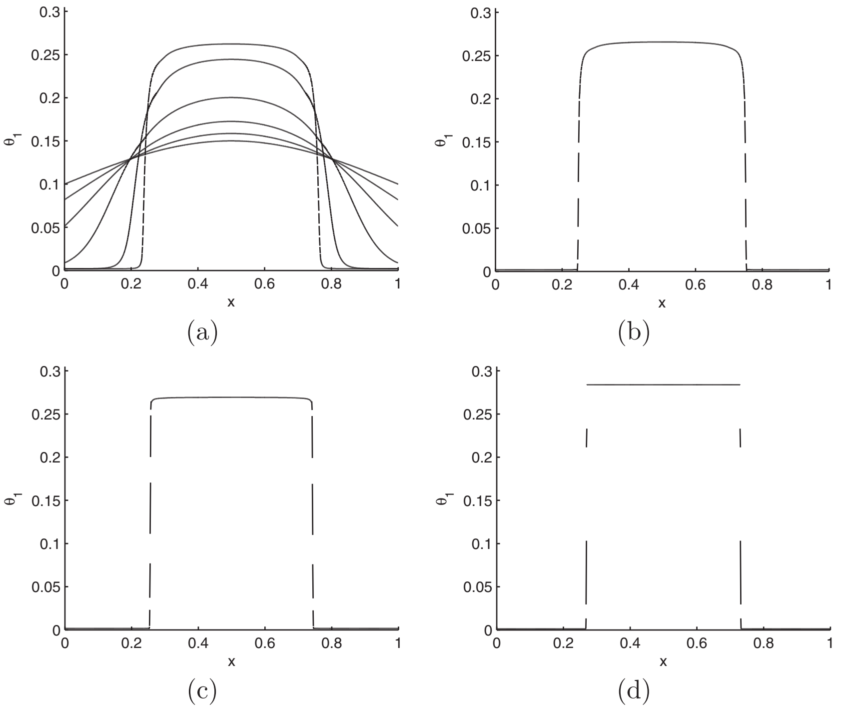

(a) (b)

(c) (d)

FIG. 1. *The volume fraction of phase* 1 *calculated from the coupled discontinuous Galerkin finite element method applied to the problem described in section* 4.1. *One thousand equally sized elements in space were used. In* (a) *we plot the volume fraction of phase* 1 *at times* $t = 0, 5, 10, 15, 20, 25$. *In* (b) *we plot the volume fraction of phase* 1 *at time* $t = 30$, *in* (c) *at time* $t = 40$, *and in* (d) *at time* $t = 500$.

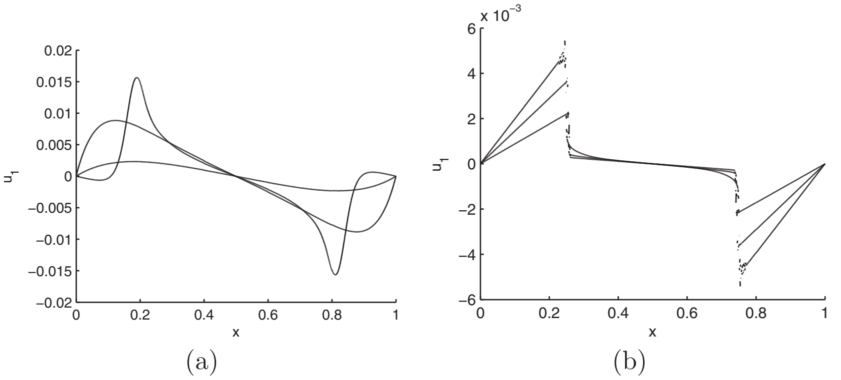

(a) (b)

FIG. 2. *The velocity of phase* 1 *calculated from the coupled discontinuous Galerkin finite element method applied to the problem described in section* 4.1. *One thousand equally sized elements in space were used. In* (a) *we plot the velocity of phase* 1 *at times* $t = 0, 10, 20$. *In* (b) *we plot the velocity of phase* 1 *at times* $t = 30, 40, 50$.

time $t = 500$, and we see that the solution approaches a steady state solution as time evolves. This long-time limit of the solution does indeed exhibit sharp gradients in the solution, and the coupled discontinuous Galerkin finite element method used handles these without spurious oscillations. The cell velocity, u_1, is plotted in Figure 2(a) for times $t = 0, 10, 20$, and in Figure 2(b) for times $t = 30, 40, 50$. As our finite element

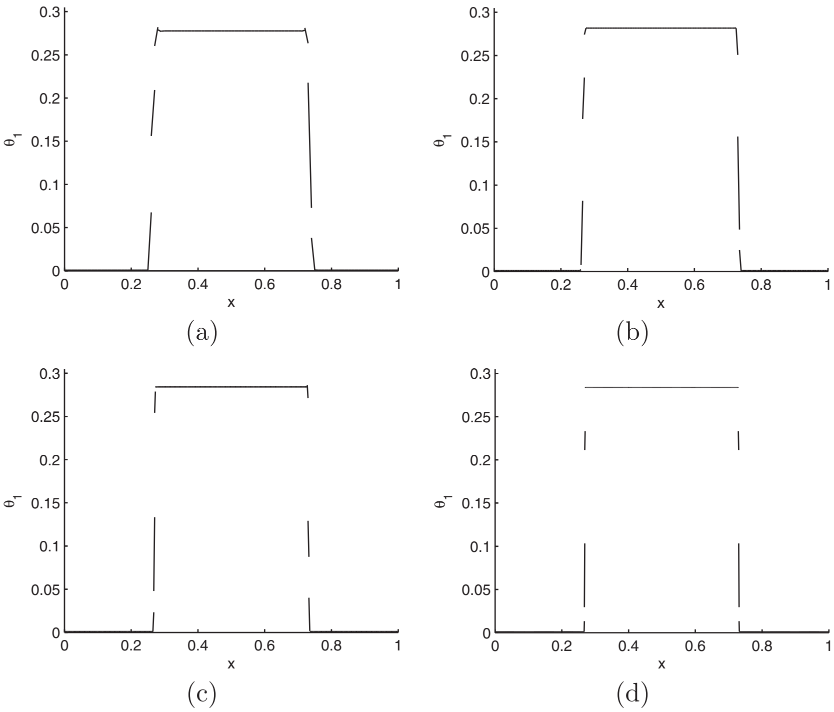

Fig. 3. *The long-time limit of the volume fraction of phase* 1 *calculated from the coupled discontinuous Galerkin finite element method applied to the problem described in section* 4.1. *In* (a) 100 *equally sized elements in space were used, in* (b) 200 *equally sized elements in space were used, in* (c) 400 *equally sized elements in space were used, and in* (d) 1000 *equally sized elements in space were used.*

method conserves the flux of cells, given by $\theta_1 u_1$, the development of sharp gradients in θ_1 exhibited in Figure 1 may generate sharp gradients in u_1 as time increases. This is seen to be the case in Figure 2(b).

In Figure 3, we demonstrate how the long-time limit of θ_1 depends on the number of (equally sized) elements in the mesh. We saw in Figure 1(d) that the solution has evolved toward a steady state at time $t = 500$, and so we take the solution at this time as the long-time limit of the solution. The solution for θ_1 at time $t = 500$ shown in Figure 3(a) was generated using 100 elements, the solution in Figure 3(b) with 200 elements, the solution in Figure 3(c) with 400 elements, and the solution in Figure 3(d) with 1000 elements. We see that all of these solutions, computed using different numbers of elements, handle the sharp gradient in θ_1 without any spurious oscillations. We also observe that, as expected, the finer meshes allow the steep gradient to be resolved more effectively: in all figures, this transient spans around three elements. As the mesh is refined, this occupies a smaller distance.

We now demonstrate the effect of changing some of the parameters in the model problem described in section 4.1. We now take $\theta_1^* = 0.8$ and use initial conditions given by $\theta_1(x,0) = 0.4 + 0.2\sin 5\pi x$, $\theta_2(x,0) = 1 - \theta_1(x,0)$. The solution for θ_1 again evolves to a long-time limit, which is shown in Figure 4(a) for 200 equally sized elements, in Figure 4(b) for 400 equally sized elements, and in Figure 4(c) for 1000 equally sized elements. The initial conditions have resulted in the solution forming three peaks, rather than one peak as in the earlier computations, and changing the value of θ_1^* has changed the height of these peaks. The solution does still, however,

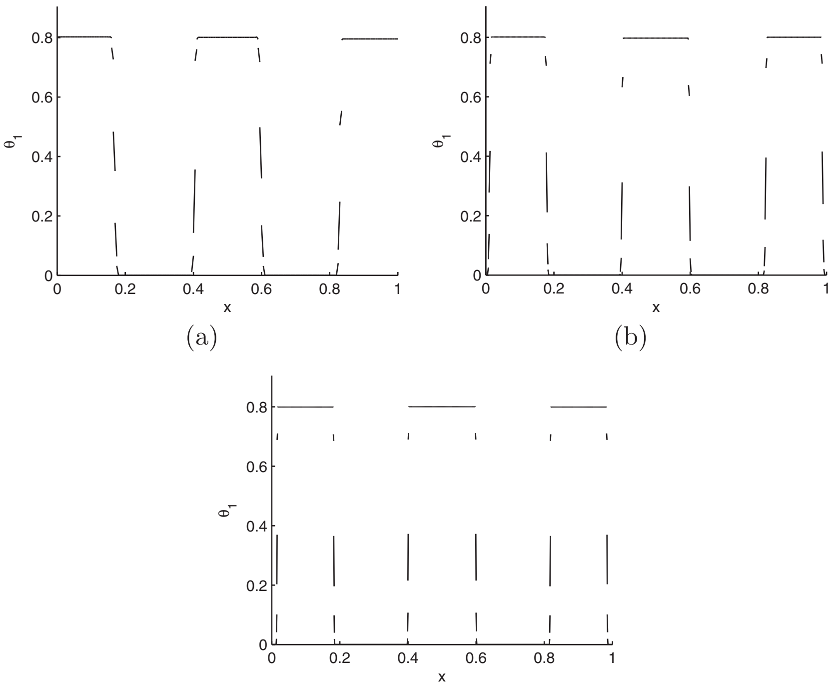

(a) (b)

(c)

Fig. 4. *The long-time limit of the volume fraction of phase* 1 *calculated from the coupled discontinuous Galerkin finite element method applied to the problem with parameters described in section* 4.1*, with the exception that* $\theta_1^* = 0.8$*, and initial conditions are given by* $\theta_1(x, 0) = 0.4 + 0.2 \sin 5\pi x$*,* $\theta_2(x, 0) = 1 - \theta_1(x, 0)$*. In* (a) 200 *equally sized elements in space were used, in* (b) 400 *equally sized elements in space were used, and in* (c) 1000 *equally sized elements in space were used.*

exhibit steep gradients in θ_1 that are effectively handled by our discontinuous Galerkin finite element method.

We now investigate the effect of the second term on the right-hand side of (4.1). Recall that this term was included to prevent the volume fraction of cells reaching zero. We repeat the simulation described in section 4.1, but with $\Lambda = 0$ to neglect this term. In Figure 5, we plot the minimum of θ_1 as a function of t for the case with $\Lambda = 0$ (represented by the solid line) and for the simulation described in section 4.1 (represented by the broken line). We see that the minimum values coincide until θ_1 becomes small, after which the broken line approaches a limit. The solid line continues to decrease: if $\theta_1 = 0$, we have already explained that the governing system of equations is singular and u_1 does not exist. In the limit that $\theta_1 \to 0$, the discretized solution, together with finite precision arithmetic, eventually results in a singular system for small, rather than zero, θ_1. This is prevented by the second term on the right-hand side of (4.1) having the desired effect of preventing θ_1 from ever reaching zero, but not affecting the solution away from regions with very small θ_1.

4.1.2. The uncoupled discontinuous Galerkin finite element method.

We now verify that the uncoupled discontinuous Galerkin method is appropriate for the model problem described in section 4.1. All the computations so far have used the coupled finite element method given by (3.15), (3.16), and (3.17). In Figure 6, we instead compute the solution using the uncoupled finite element method given by

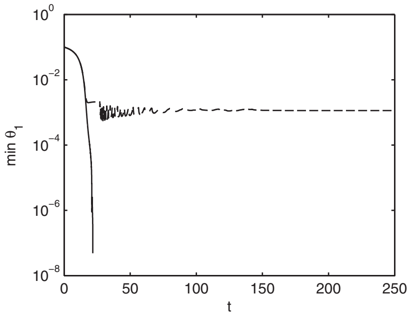

FIG. 5. *The minimum value of θ_1 as a function of t. The broken line represents the solution of the problem with parameters described in section* 4.1. *The solid line uses the same parameters with the exception that $\Lambda = 0$.*

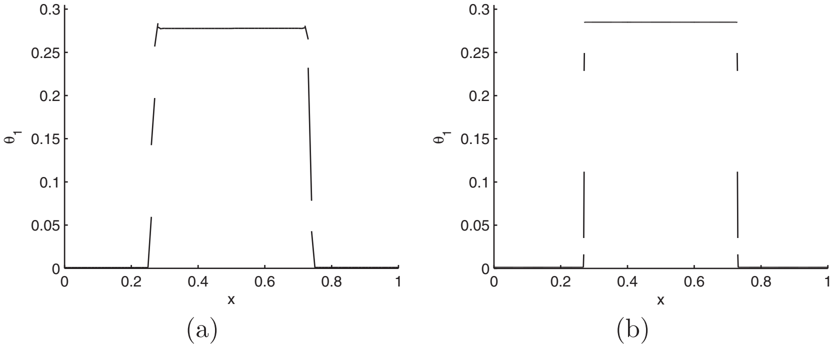

(a) (b)

FIG. 6. *The volume fraction of phase* 1 *calculated from the uncoupled discontinuous Galerkin finite element method applied to the problem described in section* 4.1. *In* (a) 100 *equally sized elements in space were used, and in* (b) 1000 *equally sized elements in space were used.*

(3.18), (3.19), and (3.20). In Figure 6(a), we plot the long-time solution using 100 equally sized elements in space, and in Figure 6(b), we plot the long-time solution using 1000 equally sized elements in space. We see on comparing with the corresponding plots for the coupled scheme—Figure 3(a) and Figure 3(d)—that there is no visible difference between the two methods.

4.1.3. Rate of convergence of the discontinuous Galerkin finite element method. Establishing the rate of convergence for discontinuous Galerkin finite element methods is still an open question in many cases, with the rate of convergence depending on a number of factors such as the degree of approximating polynomial used, the size and shape of the elements used, the norm in which convergence rate is of interest, and the discontinuous Galerkin finite element scheme used. For example, using Poisson's equation on the unit square as a test problem, with a uniform mesh of squares with edges of length h and approximating polynomial of degree p, Houston, Schwab, and Süli [19] found that the L^2-norm of the error behaves like $\mathcal{O}(h^{p+1})$ for odd p and like $\mathcal{O}(h^p)$ for even p. Yet, for the same problem, use of both odd and even p yielded a convergence rate of $\mathcal{O}(h^p)$ in an energy norm.

We now estimate the rate of convergence of the simulation described in section 4.1. We first compute a reference solution using a spatial mesh with 4096 elements and timestep of 10^{-4} and will denote the volume fraction of phase 1 of this solution by

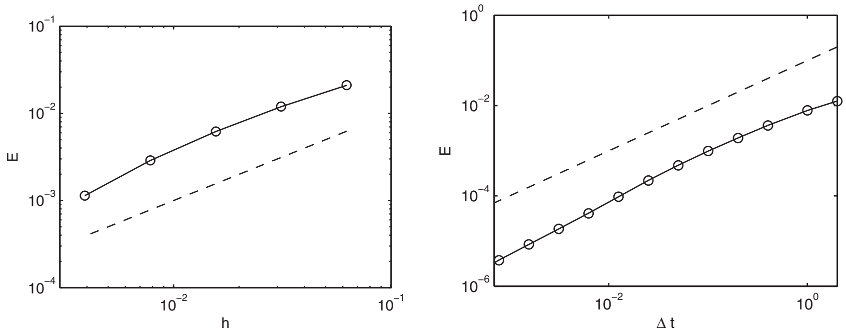

(a) (b)

FIG. 7. *The effect of both granularity of the spatial mesh and the timestep on the error in the discontinuous Galerkin solution at* $x = 0, t = 10$ *for the simulation described in section* 4.1. (a) *shows the effect of element size h, and* (b) *shows the effect of the timestep* Δt. *In both cases, the solid line represents* $E = \mid \theta_1(0, 10) - \theta_1^{h,\Delta t}(0, 10) \mid$, *and the broken line has slope* 1.

$\theta_1(x, t)$. Using the solution computed with this fine spatial mesh and short timestep as an approximation to the true solution, we then calculate the solution on coarser meshes with timestep 10^{-4} to investigate the spatial convergence of the solution. We also calculate the solution on the mesh with 4096 spatial elements with longer timesteps to investigate the temporal convergence of the solution. Denoting the finite element solution for phase 1, calculated with element size h and timestep Δt, by $\theta_1^{h,\Delta t}(x, t)$ we may calculate the difference between these solutions at $x = 0$, $t = 10$ and calculate an error $E = \mid \theta_1(0, 10) - \theta_1^{h,\Delta t}(0, 10) \mid$. In Figure 7(a), we use $\Delta t = 10^{-4}$ and plot, on logarithmic scales, the variation of E with h (solid line). In this plot, the broken line has slope 1. In Figure 7(b), we use 4096 elements and plot, again on logarithmic scales, the variation of E with Δt (solid line). The broken line on this plot again has slope 1. We see that the quantity E, calculated using the discontinuous Galerkin finite element method, has first order convergence with both h and Δt.

4.2. The limitations of the continuous Galerkin finite element method. We have demonstrated in Figures 1 and 4 that the simulations described in section 4.1 all exhibit sharp gradients in θ_1 as time evolves. The variable θ_1 satisfies the first order hyperbolic partial differential equation given by (2.2). One of our reasons for developing a discontinuous Galerkin finite element method was to use the stabilization capabilities of this method to avoid the spurious oscillations in the solution often seen when using the continuous Galerkin finite element method for hyperbolic problems. We now demonstrate that the continuous Galerkin finite element method will indeed encounter difficulties when used for the model problem described in section 4.1. We use a quadratic approximation on each element for the velocity of each phase, use a linear approximation on each element for the volume fraction of each phase and for the pressure, and use 1000 equally sized elements. In Figure 8(a), we plot the solution at time $t = 24$. We see that the solution has evolved in a similar manner to the discontinuous Galerkin finite element solution shown in Figure 1. However, when we zoom in to the region $0.24 < x < 0.26$ in Figure 8(b), we see that oscillations in the solution are beginning to develop. At a time shortly after this, the magnitude of the oscillations grew, and θ_1 took a negative value at some points. This is clearly unphysical, and Newton's method for solving the resulting system of discretized nonlinear algebraic equations failed, thus preventing us from evolving the solution fully

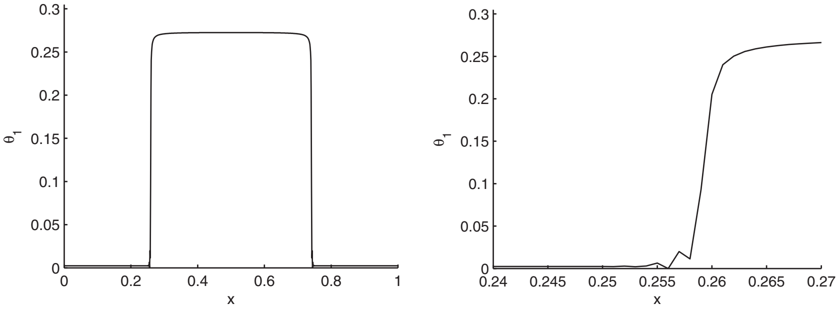

(a) (b)

Fig. 8. (a) *The volume fraction of phase* 1 *calculated from the coupled continuous Galerkin finite element method applied to the problem described in section* 4.1 *at time* $t = 24$. (b) *The* x*-axis in plot* (a) *expanded to show the development of oscillations.*

in time. This was not observed for any of the computations using the discontinuous Galerkin finite element method presented in this study.

4.3. Two-dimensional computations using the discontinuous Galerkin finite element method.

We now demonstrate the application of the uncoupled version of the discontinuous Galerkin finite element method to computations in two spatial dimensions. We use the same constitutive relations and parameters as for the one-dimensional computations described in section 4.1.

4.3.1. Computations on a structured, regular mesh.

In all simulations in this section, we use the domain $0 < x, y < L$, where $L = 0.05$, and discretize this domain into the uniform mesh of 50×50 quadrilateral elements shown in Figure 9(a).

For our first computation, we use initial conditions

$$\theta_1^{(0)}(x,y) = 0.05 + 0.1 \sin\frac{\pi x}{L} \sin\frac{\pi y}{L}, \tag{4.2}$$

$$\theta_2^{(0)}(x,y) = 1 - \theta_1^{(0)}(x,y) \tag{4.3}$$

and apply periodic boundary conditions across all boundaries. We plot the solution for $\theta_1(x, y)$ at time $t = 20$ in Figure 9(b), at time $t = 40$ in Figure 9(c), and the long-time limit in Figure 9(d). We see that, in common with the earlier one-dimensional simulations, the solution evolves to a configuration with sharp gradients in θ_1. In this two-dimensional case, all of phase 1 clusters at the center of the computational domain.

In Figures 10(a) and (b), we plot the velocity of phase 1 at times $t = 20$ and $t = 40$. These velocities are shown at the same points in time as the solutions for θ_1 shown in Figures 9(b) and (c). In both cases, we see that, as expected, the velocity of this phase is directed toward the central cluster of phase 1 that forms in the long-time limit shown in Figure 9(d). In this long-time limit, the velocity of both phases approaches zero magnitude as would be expected for a steady state solution.

For our second computation in two dimensions, we use initial conditions given by

$$\theta_1^{(0)}(x,y) = 0.12 + 0.05 \sin\frac{\pi x}{L} \sin\frac{\pi y}{L}, \tag{4.4}$$

$$\theta_2^{(0)}(x,y) = 1 - \theta_1^{(0)}(x,y) \tag{4.5}$$

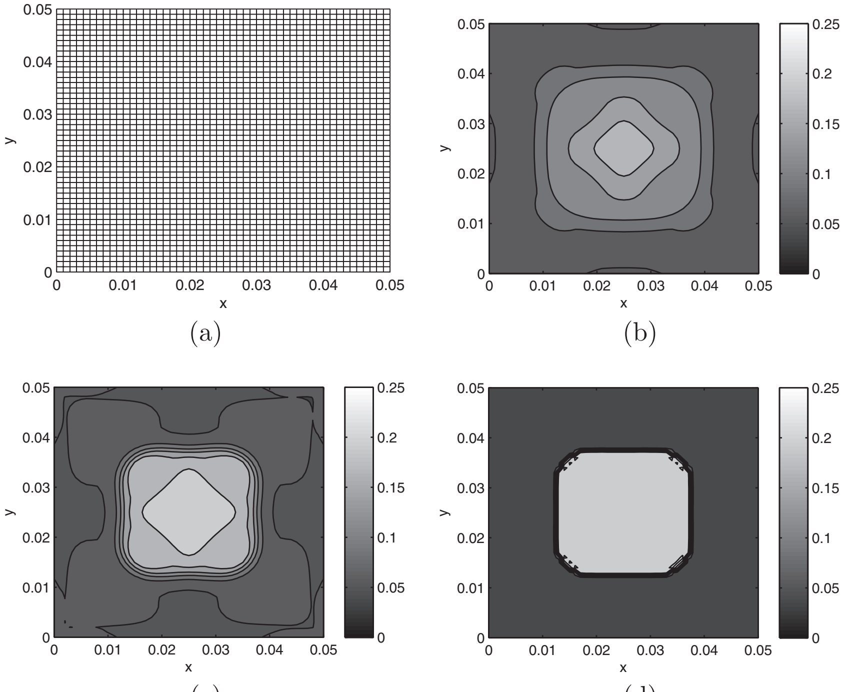

(a) (b)

(c) (d)

FIG. 9. *The volume fraction of phase* 1 *for the simulations with initial conditions given by* (4.2) *and* (4.3)*. The mesh for these simulations is shown in* (a)*.* (b) *shows the solution at time* $t = 20$*,* (c) *shows the solution at time* $t = 40$*, and* (d) *shows the long-time limit of this simulation.*

and again apply periodic boundary conditions across all edges. The long-time limit of the solution for this computation is given in Figure 11(a). We again see that the solution evolves to a solution with regions of roughly constant θ_1, patched together with sharp gradients in θ_1. As was seen in Figure 9(d), most of phase 1 clusters in the center of the computational domain in the long-time limit. In this case, there are some additional smaller clusters of phase 1 in each corner of the computational domain.

Our final computation that uses a structured, uniform mesh in two dimensions uses the initial conditions given by

$$\theta_1^{(0)}(x,y) = 0.1 + 0.05 \sin\frac{\pi x}{L} \sin\frac{4\pi y}{L}, \tag{4.6}$$

$$\theta_2^{(0)}(x,y) = 1 - \theta_1^{(0)}(x,y). \tag{4.7}$$

In contrast to the previous computations in two dimensions presented in this section, we apply zero velocity boundary conditions on all boundaries rather than periodic boundary conditions. The long-time limit of the solution for this computation is shown in Figure 11(b), and this solution again exhibits regions of roughly constant θ_1, with sharp gradients in θ_1 separating these regions. Note the small clusters of phase 1 that emerge near to some corners of the computational domain.

4.3.2. Computations on an unstructured mesh. We now investigate the effect of an unstructured computational mesh on the long-time limit of the solution.

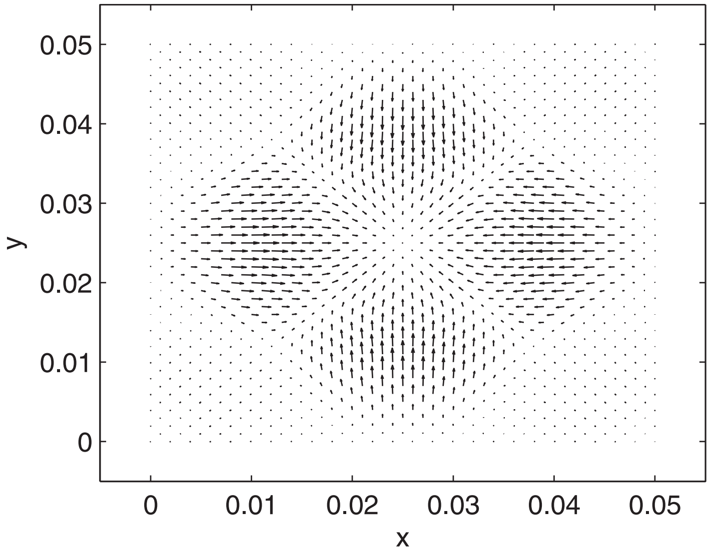

(a)

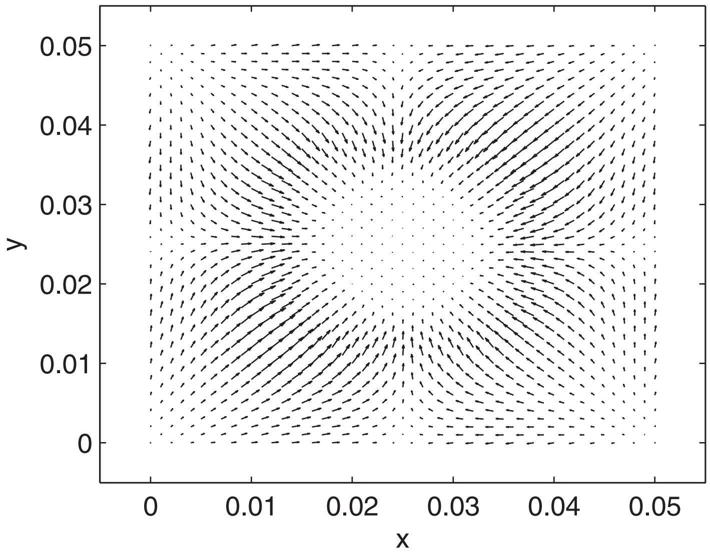

(b)

Fig. 10. *The velocity of phase* 1 *for the simulations with initial conditions given by* (4.2) *and* (4.3). (a) *the velocity at time* $t = 20$, *and* (b) *the velocity at time* $t = 40$. *At each point, the arrow shows the direction of the velocity, with the magnitude of the velocity being proportional to the length of the arrow.*

We generate the unstructured mesh shown in Figure 12(a) by adding random perturbations in both x and y to each node of the uniform mesh shown in Figure 9(a). We then repeat the simulation with initial conditions given by (4.2) and (4.3) and apply periodic boundary conditions across all boundaries. The long-time limit of the solution is shown in Figure 12(b). Comparing this long-time limit with that computed on a uniform mesh and shown in Figure 9(d), we see that the accuracy of the solu-

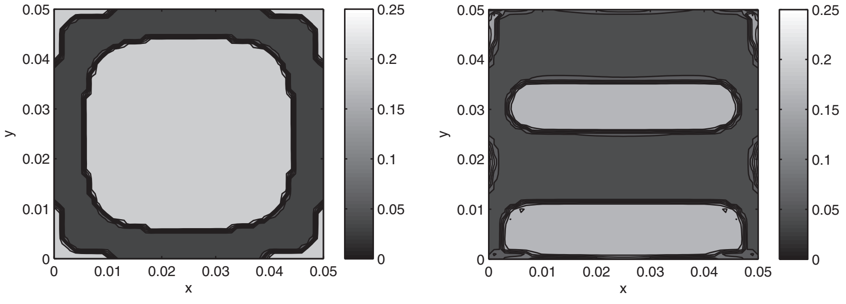

(a) (b)

Fig. 11. *The long-time limit of the volume fraction of phase* 1. *In* (a)*, the initial conditions are given by* (4.4) *and* (4.5)*. In* (b)*, the initial conditions are given by* (4.6) *and* (4.7)*.*

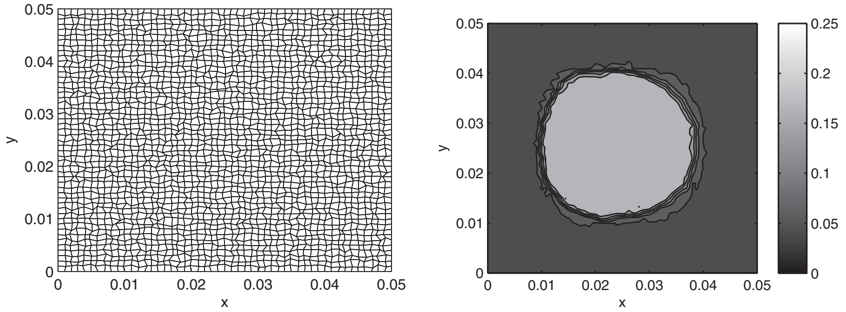

(a) (b)

Fig. 12. *The simulation described in section* 4.3.2 *with initial conditions given by* (4.2) *and* (4.3)*.* (a) *the mesh used for these simulations.* (b) *the long-time limit of the volume fraction of phase* 1*.*

tion is degraded by the low quality mesh (as would be expected), but the qualitative distribution—regions of roughly constant θ_1, with sharp gradients of θ_1 between these regions—is unchanged.

4.3.3. Computations on an irregular region. We now consider simulations on an irregular region. This region is generated by taking the region $0 < X, Y < L$ and warping using the map

$$x = X + \frac{Y^2}{(1.01L)^2}(2L - X), \qquad y = Y. \tag{4.8}$$

To also allow the effect of anisotropic meshes to be investigated, the computational mesh used is a uniform 50×50 mesh in (X, Y) coordinates that is mapped onto (x, y) coordinates using the map given by (4.8). Taking $L = 0.05$ gives the computational domain and mesh shown in Figure 13(a). Defining the aspect ratio of an element to be the ratio of the longest edge to the shortest edge, this mesh has a maximum aspect ratio of 203. We take initial conditions

$$\theta_1^{(0)}(x, y) = 0.1 + 0.05 \sin\frac{2\pi X}{L} \sin\frac{\pi Y}{L}, \tag{4.9}$$

$$\theta_2^{(0)}(x, y) = 1 - \theta_1^{(0)}(x, y), \tag{4.10}$$

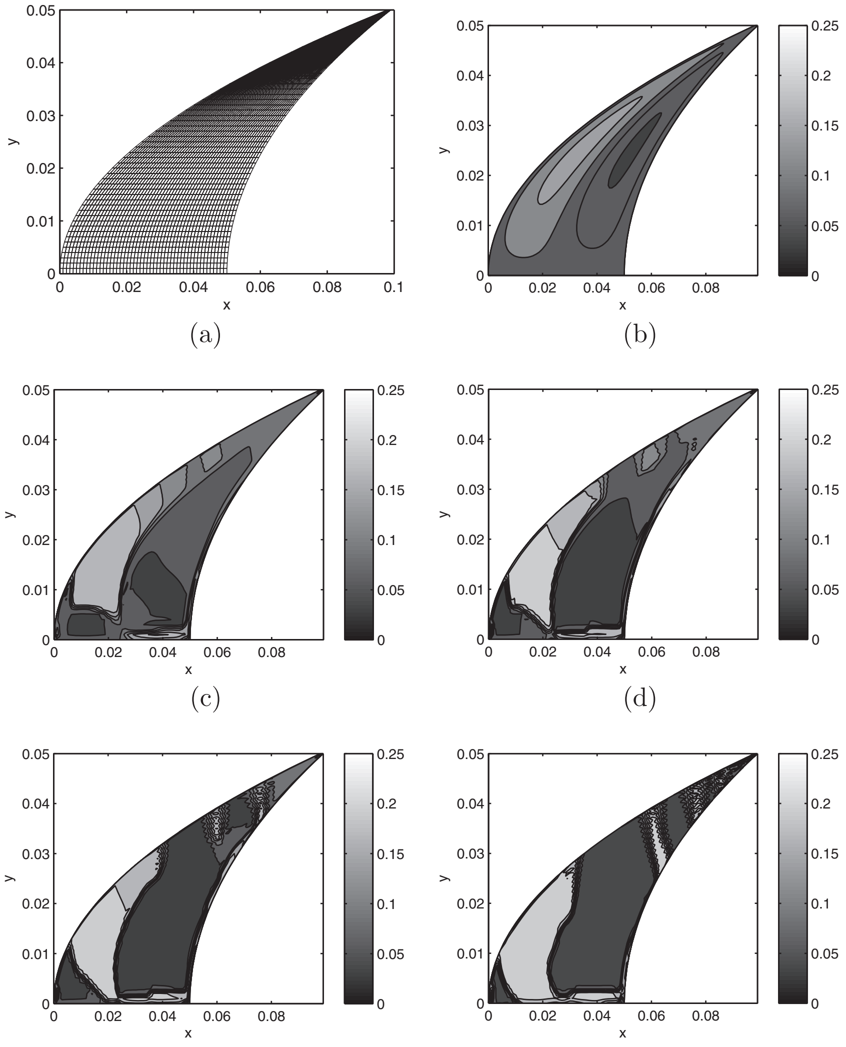

(a) (b)

(c) (d)

(e) (f)

FIG. 13. *The volume fraction of phase* 1 *for the simulation described in section* 4.3.3. (a) *The domain and computational mesh,* (b) *the volume fraction of phase* 1 *at time* $t = 0$, (c) *the volume fraction of phase* 1 *at time* $t = 10$, (d) *the volume fraction of phase* 1 *at time* $t = 20$, (e) *the volume fraction of phase* 1 *at time* $t = 30$, *and* (f) *the volume fraction of phase* 1 *in the long-time limit.*

where X, Y, x, y are related by (4.8). We apply zero velocity boundary conditions on all boundaries and use the same parameters and constitutive relations as those used in section 4.1.

We plot the initial conditions given by (4.9) and (4.10) in Figure 13(b). The solution at times $t = 10, 20, 30$ is plotted in Figures 13(c), (d), and (e), and the long-time limit is plotted in Figure 13(f). As before, the solution evolves toward regions of roughly constant θ_1 that are linked together through thin regions that contain rapid variations in θ_1. We note that no problems with stability were encountered when using the anisotropic mesh shown in Figure 13(a).

5. Discussion. In this study, we have developed a discontinuous Galerkin finite element method that may be used to compute a finite element solution of the equations governing multiphase viscous flow. This finite element method was applied to the exemplar application of a simple mathematical model of the evolution of the spatial distribution of biological cells. The solution to this model problem exhibits sharp gradients in the volume fractions of the phases in the long-time limit. The finite element solutions computed using the algorithm developed in this study did not exhibit any instabilities despite the evolution of these sharp gradients, allowing the demonstration of patterning behavior as the spatial distribution of cells evolves. The solutions presented in this study were all computed using a timestep that was dictated by accuracy considerations. Longer timesteps degraded the accuracy of the solution as would be expected. However, the timestep had to be increased to be orders of magnitude longer than that needed for accuracy considerations before the positivity of the volume fractions was violated.

The discontinuous Galerkin finite element method described in this study is clearly suitable for calculating the finite element solution of the exemplar model problems considered. Implementing this finite element method does, however, require a more advanced understanding of the finite element method than is needed when implementing the continuous Galerkin finite element method. It is therefore natural to ask whether the continuous Galerkin finite element method would also be suitable for computing a numerical solution of the governing equations. In contrast to the continuous Galerkin finite element method, the discontinuous Galerkin finite element method was derived by enforcing, in the weak sense, continuity of both the flux and the stress of all phases across interior element boundaries. The continuous Galerkin finite element method assumes, instead, that all variables are continuous across element boundaries. We have seen in our computations that very rapid spatial changes in the volume fraction of a phase may develop as time evolves. The discontinuous Galerkin finite element method allows these rapid changes to be computed as discontinuities in the solution and thus handles these rapid changes very effectively. Difficulties were encountered when using the continuous Galerkin finite element method for these problems as enforcing continuity of these rapidly varying volume fractions resulted in spurious oscillations that generate physically nonsensical negative volume fractions.

REFERENCES

[1] A. D. Fitt, P. D. Howell, J. R. King, C. P. Please, and D. W. Schwendeman, *Multiphase flow in a roll press nip*, European J. Appl. Math., 13 (2002), pp. 225–259.

[2] M. G. Worster, *Natural convection in a mushy layer*, J. Fluid Mech., 224 (1991), pp. 335–359.

[3] L. Preziosi, D. D. Joseph, and G. S. Beavers, *Infiltration of initially dry, deformable porous media*, Int. J. Multiphase Flow, 22 (1996), pp. 1205–1222.

[4] B. G. Sengers, C. W. J. Oomens, and F. P. T. Baaijens, *An integrated finite–element approach to mechanics, transport and biosynthesis in tissue engineering*, J. Biomech. Eng., 126 (2004), pp. 82–91.

[5] H. P. Greenspan, *Models for the growth of a solid tumour by diffusion*, Stud. Appl. Math., 52 (1972), pp. 317–340.

[6] C. J. W. Breward, H. M. Byrne, and C. E. Lewis, *A multiphase model describing vascular tumour growth*, Bull. Math. Biol., 65 (2003), pp. 609–640.

[7] J. M. Oliver, J. R. King, K. J. McKinlay, P. D. Brown, D. M. Grant, C. A. Scotchford, and J. V. Wood, *Thin–film theories for two–phase reactive flow models of active cell motion*, Math. Med. Biol., 22 (2005), pp. 53–98.

[8] A. Häcker, *A mathematical model for mesenchymal and chemosensitive cell dynamics*, J. Math. Biol. 64 (2012), pp. 361–401.

[9] J. M. Osborne, R. D. O'Dea, J. P. Whiteley, H. M. Byrne, and S. L. Waters, *The influence of bioreactor geometry and the mechanical environment on engineered tissues*, J. Biomech. Eng., 132 (2010), 051006.

[10] M. E. Hubbard and H. M. Byrne, *Multiphase modelling of vascular tumour growth in two spatial dimensions*, J. Theoret. Biol., 316 (2013), pp. 70–89.

[11] J. M. Osborne and J. P. Whiteley, *A numerical method for the multiphase viscous flow equations*, Comput. Methods Appl. Mech. Engrg., 199 (2010), pp. 3402–3417.

[12] B. Cockburn and C.-W. Shu, *The local discontinuous Galerkin method for time–dependent convection–diffusion systems*, SIAM J. Numer. Anal., 35 (1998), pp. 2440–2463.

[13] P. Houston and E. Süli, *hp-adaptive discontinuous Galerkin finite element methods for first–order hyperbolic problems*, SIAM J. Sci. Comput., 23 (2001), pp. 1226–1252.

[14] R. Hartmann and P. Houston, *Adaptive discontinuous Galerkin finite element methods for nonlinear hyperbolic conservation laws*, SIAM J. Sci. Comput., 24 (2002), pp. 979–1004.

[15] E. H. Georgoulis, *hp-version interior penalty discontinuous Galerkin finite element methods on anisotropic methods*, Int. J. Numer. Anal. Model., 3 (2006), pp. 52–79.

[16] E. H. Georgoulis, E. Süli, and P. Houston, *Discontinuous Galerkin methods for advection–diffusion–reaction problems on anisotropically refined meshes*, SIAM J. Sci. Comput., 30 (2007), pp. 246–271.

[17] R. Hartmann and P. Houston, *Adaptive discontinuous Galerkin finite element methods for the compressible Euler equations*, J. Comput. Phys., 183 (2002), pp. 508–532.

[18] P. Houston, B. Senior, and E. Süli, *hp-discontinuous Galerkin finite element methods for hyperbolic problems: Error analysis and adaptivity* I, J. Numer. Methods Fluids, 40 (2002), pp. 153–169.

[19] P. Houston, C. Schwab, and E. Süli, *Discontinuous hp-finite element methods for advection–diffusion–reaction problems*, SIAM J. Numer. Anal., 39 (2002), pp. 2133–2163.

[20] P. Houston, D. Schötzau, and T. P. Wihler, *An hp-adaptive mixed discontinuous Galerkin FEM for nearly incompressible linear elasticity*, Comput. Methods Appl. Mech. Engrg., 195 (2006), pp. 3224–3246.

[21] P. Houston, E. Süli, and T. P. Wihler, *A posteriori error analysis of hp-version discontinuous Galerkin finite–element methods for second–order quasi–elliptic PDEs*, IMA J. Numer. Anal., 28 (2008), pp. 245–273.

[22] J. P. Whiteley, *Discontinuous Galerkin finite element methods for incompressible non–linear elasticity*, Comput. Methods Appl. Mech. Engrg., 198 (2009), pp. 3464–3478.

[23] D. Schötzau, C. Schwab, and A. Toselli, *Mixed hp-DGFEM for incompressible flows*, SIAM J. Numer. Anal., 40 (2003), pp. 2171–2194.

[24] V. Girault, B. Rivière, and M. F. Wheeler, *A discontinuous Galerkin method with nonlinear domain decomposition for the Stokes and Navier–Stokes problems*, Math. Comp., 74 (2004), pp. 53–84.

[25] B. Cockburn, D. Schötzau, and J. Wang, *Discontinuous Galerkin methods for incompressible elastic materials*, Comput. Methods Appl. Mech. Engrg., 195 (2006), pp. 3184–3204.

[26] P. Hansbo and M. G. Larson, *Discontinuous Galerkin methods for incompressible and nearly incompressible elasticity by Nitsche's method*, Comput. Methods Appl. Mech. Engrg., 191 (2002), pp. 1895–1908.

[27] A. Ten Eyck and A. Lew, *Discontinuous Galerkin methods for non–linear elasticity*, Internat. J. Numer. Methods Engrg., 67 (2006), pp. 1204–1243.

[28] G. Lemon, J. R. King, H. M. Byrne, O. E. Jensen, and K. M. Shakesheff, *Mathematical modelling of engineered tissue growth using a multiphase porous flow mixture theory*, J. Math. Biol., 52 (2006), pp. 571–594.

[29] L. W. Schwartz and R. R. Eley, *Simulation of droplet motion on low–energy and heterogeneous surfaces*, J. Colloid Interface Sci., 202 (1998), pp. 173–188.